REPORT DOCUMENTATION PAGE

PLEASE DO NOT RETURN YOUR FORM TO THE ABOVE ORGANIZATION.

1. REPORT DATE	2. REPORT TYPE	3. DATES COVERED	
		START DATE	END DATE
20220103	Conference Paper with Briefing Charts	20211110	20220131

4. TITLE AND SUBTITLE

Conjugate Heat Transfer Analysis of the Wall Heat Flux in a Liquid Rocket Engine

5a. CONTRACT NUMBER	5b. GRANT NUMBER	5c. PROGRAM ELEMENT NUMBER
5d. PROJECT NUMBER	**5e. TASK NUMBER**	**5f. WORK UNIT NUMBER**
		Q24U

6. AUTHOR(S)

Matthew Harvazinski, Tomas Houba

7. PERFORMING ORGANIZATION NAME(S) AND ADDRESS(ES)

Air Force Research Laboratory (AFMC)
AFRL/RQRC
10 E. SATURN BLVD,
EDWARDS AFB, CA 93524-7680

8. PERFORMING ORGANIZATION REPORT NUMBER

9. SPONSORING/MONITORING AGENCY NAME(S) AND ADDRESS(ES)	10. SPONSOR/MONITOR'S ACRONYM(S)	11. SPONSOR/MONITOR'S REPORT NUMBER(S)
Air Force Research Laboratory (AFMC), AFRL/RQR 5 Pollux Drive Edwards AFB, CA 93524-7048		AFRL-RQ-ED-TP-2021-286

12. DISTRIBUTION/AVAILABILITY STATEMENT

TP: Distribution Statement A: Approved for Public Release; Distribution is Unlimited. PA Clearance Number: AFRL-2021-4161 ; Clearance Date: 23NOV21

VG: Distribution Statement A: Approved for Public Release; Distribution is Unlimited. PA Clearance Number: AFRL-2021-4162; Clearance Date: 23NOV21

13. SUPPLEMENTARY NOTES

For presentation at AIAA SciTech 2022; January 3,2022; San Diego, CA

The U.S. Government is joint author of the work and has the right to use, modify, reproduce, release, perform, display, or disclose the work. Prepared in collaboration with Sierra Lobo Inc.

14. ABSTRACT

The accurate prediction of the wall heat flux in liquid rocket engines is critical to the design of the engine and its thermal management. The measurement of the wall heat flux in liquid rocket engines is difficult to obtain experimentally. Computational tools often utilize an adiabatic thermal boundary condition which makes the prediction of wall heat flux impossible. In the present work, we apply a conjugate heat transfer model which couples the solid conduction in the wall with the fluid dynamics in the combustor.

15. SUBJECT TERMS

16. SECURITY CLASSIFICATION OF:			17. LIMITATION OF ABSTRACT	18. NUMBER OF PAGES
a. REPORT	b. ABSTRACT	C. THIS PAGE		
Unclassified	Unclassified	Unclassified	SAR	34

19a. NAME OF RESPONSIBLE PERSON	19b. PHONE NUMBER *(Include area code)*
Matthew Harvazinski	N/A

PREVIOUS EDITION IS OBSOLETE.

STANDARD FORM 298 (REV. 5/2020)
Prescribed by ANSI Std. Z39.18

Conjugate Heat Transfer Analysis of the Wall Heat Flux in a Liquid Rocket Engine

Matthew E. Harvazinski*
AFRL, Edwards AFB, CA, 93536

Tomas Houba†
Sierra Lobo Inc., Edwards AFB, CA, 93536

The accurate prediction of the wall heat flux in liquid rocket engines is critical to the design of the engine and its thermal management. The measurement of the wall heat flux in liquid rocket engines is difficult to obtain experimentally. Computational tools often utilize an adiabatic thermal boundary condition which makes the prediction of wall heat flux impossible. In the present work, we apply a conjugate heat transfer model which couples the solid conduction in the wall with the fluid dynamics in the combustor. The validity of the solid conduction model is verified using exact solutions. The conjugate heat transfer model is applied to a H_2-O_2 rocket engine combustor. The developed computational model predicts the experimentally measured heat flux within 4% for three of the four operating conditions.

I. Introduction

Liquid rocket engine combustors are a high temperature and high-pressure environment. These conditions can push the limits of material properties and often require sophisticated cooling solutions. The recent push for reusability puts further constraints on the design of liquid rocket engines by requiring increased service life and minimization of post-flight inspection and service[1]. Reusability may also place new requirements on analysis tools including thermal fatigue and the interaction between thermal, fluids, and structural elements[2]. This type of analysis will require accurate inputs, which at a minimum will include surface temperature and heat flux measurements. The accurate determination of wall heat fluxes and surface temperatures is difficult. This type of analysis will require accurate inputs, which at a minimum will include surface temperature and heat flux measurements.

The accurate determination of wall heat fluxes and surface temperatures is difficult. Experimentally these are harsh environments that can be difficult to instrument. Heat-flux data from sub-scale experiments are frequently in the form of calorimetry data. In a calorimetry experiment, the enthalpy change in water flowing through a wall section is equivalent to the amount of heat transferred from the combustor to the wall section [3].This of course is only true in thermal equilibrium, so it is difficult to obtain transient heat flux data. Other methods include inverse methods where a series of thermocouples at a known spacing are used to compute the temperature gradient in the solid wall[4].

Computational studies often neglect wall heat transfer by using adiabatic wall boundary conditions. This results in higher combustor temperatures and large over predictions in the wall temperatures[5]. The traditional adiabatic wall boundary condition also prohibits a prediction of the wall heat flux. Relaxing the adiabatic assumption requires information that is typically not available, either the wall temperature or heat flux. These quantities can be functions of the location and run time. Numerically, the predictability of wall temperature and heat flux can be achieved by including a model for temperature inside the solid wall as part of the solution. The conjugate heat transfer problem is numerically expensive because the numerical resolution of the flowfield near the wall must be extremely fine to capture the strong thermal gradient present adjacent to the wall. This thermal gradient can introduce changes in the species composition which must be included at an extra cost. Finally, the time scales associated with conduction in the solid wall are orders of magnitude above typical simulation times. This separation in scales often leads to decoupled solutions where the fluid and solid are solved separately.

In this work we build a conjugate heat transfer capability that can interface with a reacting flow solver. The solid conduction solver is verified using several exact solutions. Finally, the prediction of wall heat flux is verified using experimental data which measured the heat flux as a function of chamber pressure for a H_2-O_2 liquid rocket engine combustor.

*Senior Aerospace Engineer, AIAA Senior Member.
†Aerospace Engineer, AIAA Member.

II. Computational Framework for Conduction and Conjugate Heat Transfer

For this work, the GEMS solver is used. GEMS is an in-house finite volume solver which is second-order accurate in time and space. It solves the reacting Navier-Stokes equations using RANS, DES, or LES turbulence models in two- and three-dimensions[6–9]. For the present study two-dimensional unsteady RANS is used. To overcome the lack of information about the wall temperature a conjugate heat transfer model has been developed. This requires two modifications. First, the solver must be configured to solve for the conduction heat transfer in the solid wall, and second, communication between the two domains must be achieved. To address the first modification, the solver was modified to solve only the energy equation in selected domains. Domains are tagged during mesh generation as either a solid or fluid zone. The fluid zone solves the standard fluids equations while the solid zone solves only the energy equation. For simplicity, the same energy equation is used in both the fluid and solid zones,

$$\rho \frac{\mathrm{D}h^0}{\mathrm{D}t} = \frac{\partial p}{\partial t} - \frac{\partial}{\partial x_i}\left(-\lambda \frac{\partial T}{\partial x_i} + \rho \sum_{k=1}^{N} h_k Y_k V_{k,i}\right) + \frac{\partial}{\partial x_j}\left(\tau_{ij} u_i\right) \tag{1}$$

In the solid domain, $\mathbf{u} = 0$, $Y_k = 0$, and $p = \text{const}$. These simplifications reduce the energy equation to:

$$\rho \frac{\partial h^0}{\partial t} = \frac{\partial}{\partial x_i}\left(\lambda \frac{\partial T}{\partial x_i}\right) \tag{2}$$

Additionally, we augment the solid with an equation of state:

$$\rho = \text{const} \qquad \lambda = \text{const} \qquad c_p = \text{const} \tag{3}$$

$$h^0 = c_p T \tag{4}$$

$$\alpha = \frac{\lambda}{\rho c_p} \tag{5}$$

These simplifications reduce the energy equation in the solid to the standard heat equation,

$$\frac{\partial T}{\partial t} = \alpha \frac{\partial^2 T}{\partial x_i^2}$$

At the interface between the fluid domain and the solid domain, we must enforce the no-slip velocity condition in the fluid domain. A matching of the heat fluxes at the interface is usef for the thermal boundary condition in each domain,

$$\lambda_f \frac{\partial T_f}{\partial \hat{n}} = \lambda_s \frac{\partial T_s}{\partial \hat{n}} \tag{6}$$

where $\hat{n}$ is the direction normal to the face. Equation 6 states that the heat flux leaving one domain must equal the heat flux entering the other domain. In the current implementation, the time step in both domains is identical and the boundary matching condition is enforced at every time step. This is considered a tightly coupled system. Figure 1 shows a sketch of the solid-fluid interface. To determine the temperature at the interface, T_w, and the heat flux, q''_w, we express the heat flux using one-sided differences,

$$\lambda_f \frac{T_f - T_w}{d_f} = \lambda_s \frac{T_w - T_s}{d_s} \tag{7}$$

Solving for T_w we obtain,

$$T_w = \frac{\frac{\lambda_f}{d_f} T_f + \frac{\lambda_s}{d_s} T_s}{\frac{\lambda_f}{d_f} + \frac{\lambda_s}{d_s}} \tag{8}$$

Once the wall interface temperature is computed, the heat flux is computed using,

$$q''_w = \lambda_s \frac{T_w - T_s}{d_s} \tag{9}$$

It is also possible to compute the heat flux from the fluid domain using a similar definition, in the current implementation the solid domain is used.

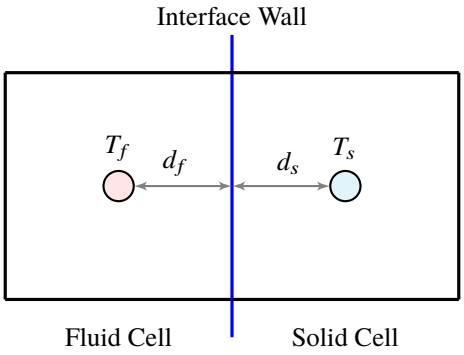

Fig. 1 The interface between the fluid domain and solid domain. T_f is the fluid temperature and T_s is the solid temperature. d_f and d_s represent the distances from the cell center to the interface face.

III. Verification of Solid Conduction

Before attempting a full conjugate solution, the accuracy of the solid conduction model is evaluated using several exact solutions. The targeted application uses copper for the solid wall, therefore each test case is run with the following physical properties[10]:

$$\rho = 8933 \frac{\text{kg}}{\text{m}^3}$$
$$\lambda = 401 \frac{\text{W}}{\text{m} \cdot \text{K}}$$
$$c_p = 385 \frac{\text{J}}{\text{kg} \cdot \text{K}}$$
$$\alpha = 1.1194 \times 10^{-4} \frac{\text{m}^2}{\text{s}}$$

The description and validation results for each of these cases is presented next.

A. Case 1: Constant Temperature Boundary in a 1D Semi-infinite Solid

The solution of a specified constant temperature boundary in a 1D semi-infinite solid is[11],

$$T(x,t) = T_b + (T_i - T_b)\,\text{erf}\left(\frac{x}{\sqrt{4\alpha t}}\right) \tag{10}$$

The case setup is shown in Figure 2. The case is solved in a 2D domain with adiabatic walls on three sides, and the specified temperature boundary on the remaining side. The large aspect ratio of 20 makes this a good approximation to a semi-infinite solid. Uniform mesh resolutions of 0.01 m and 0.001 m are examined. This results in mesh sizes of 200×10 and 2000×100. The initial temperature is 300 K and the boundary temperature is 500 K. Data are compared with the exact solution at distances of 0.005 m, 0.035 m, 0.065 m, 0.095 m and 0.125 m from the heated face. The simulation is run for 20 s with a time step of 1×10^{-6} s. This time step is small compared to what is required to accurately represent solid conduction but is representative of the fluid time scale that the conjugate problem will use. The results are shown in Figure 3. There is a slight discrepancy in the temperature for the coarse mesh, on the fine mesh the computational solution overlaps with the exact solution.

B. Case 2: Constant Heat Flux Boundary in a 1D Semi-infinite Solid

The solution of a specified constant heat flux boundary in a 1D semi-infinite solid is[11],

$$T(x,t) = \frac{q''}{\lambda}\left\{\sqrt{\frac{4\alpha t}{\pi}}\exp\left(-\frac{x^2}{4\alpha t}\right) - x\,\text{erfc}\left(\frac{x}{\sqrt{4\alpha t}}\right)\right\} + T_i \tag{11}$$

The case setup is shown in Figure 4. The case is solved in a 2D domain with adiabatic walls on three sides, and the specified heat flux boundary on the remaining side. A uniform resolution of 0.01 m is examined which translates to

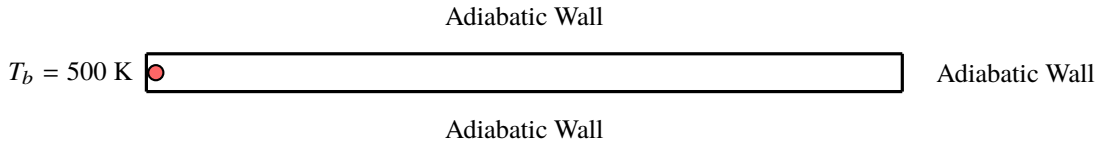

Fig. 2 Case setup for solid conduction validation case one, specified temperature. The red circle represents the furthest downstream point of comparison, 0.125 m**.**

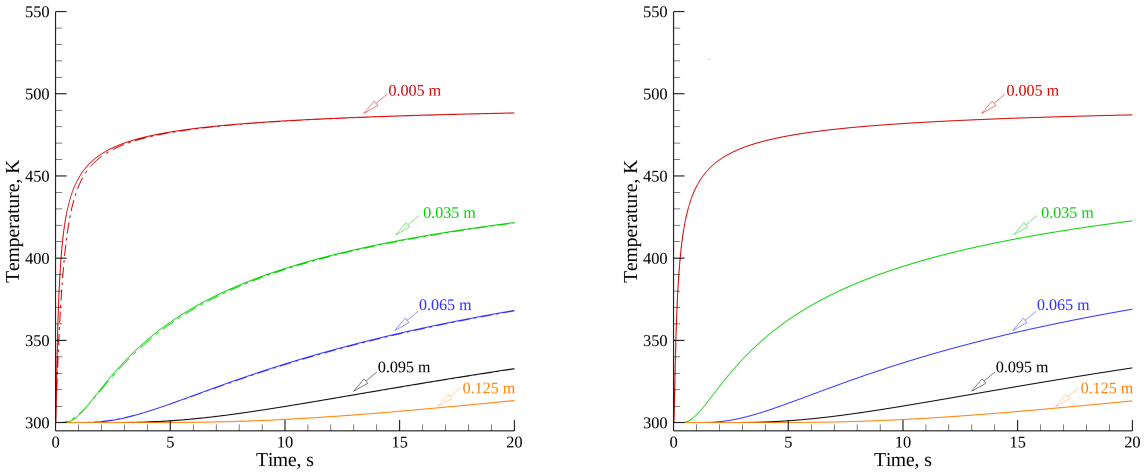

(a) Δx = 0.01 m **(b)** Δx = 0.001 m

Fig. 3 Simulation results for case 1 verification. Solid lines are simulation results and dashed lines are the exact solution.

a mesh size of 200×10. The initial temperature is 500 K and the boundary heat flux is 401×10^3 W m^{-2}. Data are compared with the exact solution at distances of 0.005 m, 0.035 m, 0.065 m, 0.095 m and 0.125 m from the heated face. The simulation is run for 20 s with a time step of 1×10^{-6} s. The results are shown in Figure 5. For this case the computational solution overlaps with the exact solution on the coarse mesh, so the case was not repeated on the fine mesh.

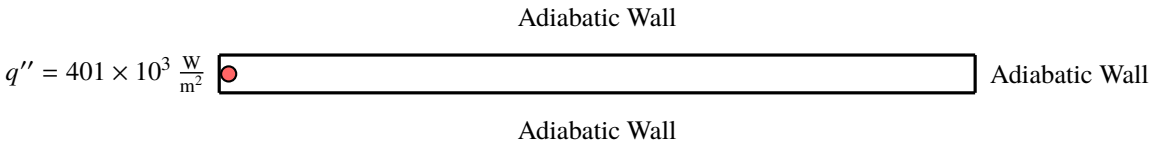

Fig. 4 Case setup for solid conduction validation case two, specified heat flux. The red circle represents the furthest downstream point of comparison 0.125 m**.**

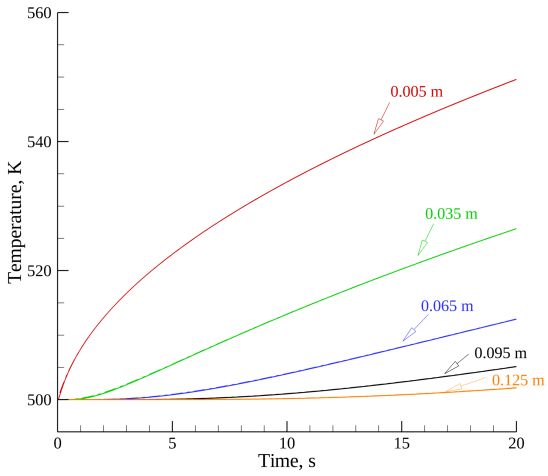

(a) $\Delta x = 0.01$ m

Fig. 5 Simulation results for case 2 verification. Solid lines are simulation results and dashed lines are the exact solution.

C. Case 3: Linear Variation of a Temperature Boundary in a 1D Semi-infinite Solid

This case is setup identical to case 1 except that the temperature at the boundary is allowed to vary as a function of time. The input temperature profile is,

$$T_b(t) = \begin{cases} 300 + 30t & 0 \leq t \leq 8 \\ 540 & 8 < t \leq 12 \\ 780 - 20t & 12 < t \leq 16 \\ 460 & t > 16 \end{cases} \tag{12}$$

The corresponding exact solution to this case is[11],

$$T(x,t) = 30\mathcal{T}(x,t) - 30\mathcal{T}(x,t-8)u(t-8) - 20\mathcal{T}(x,t-12)u(t-12) + 20\mathcal{T}(x,t-16)u(t-16) \tag{13}$$

where $u(t)$ is the Heaviside step function and,

$$\mathcal{T}(x,t) = t\left\{\left(1 + 2\frac{x^2}{4\alpha t}\right)\operatorname{erfc}\left(\frac{x}{\sqrt{4\alpha t}}\right) - \frac{2}{\sqrt{\pi}}\frac{x}{\sqrt{4\alpha t}}\exp\left(-\frac{x^2}{4\alpha t}\right)\right\} \tag{14}$$

Uniform resolutions of 0.01 m and 0.001 m are examined. This results in mesh sizes of 200×10 and 2000×100. The initial temperature is 300 K. Data are compared with the exact solution at distances of, 0.005 m, 0.035 m, 0.065 m, 0.095 m and 0.125 m from the heated face. The simulation is run for 20 s with a time step of 1×10^{-6} s. The results are shown in Figure 6. Similar to case 1, there is slight discrepancy between the computational solution and the exact solution for the coarse mesh, for the fine mesh the solutions overlap.

D. Case 4: 2D Conduction in a Solid Slab

This case is a two-dimensional problem where a constant heat flux is applied to a portion of one wall. The remaining walls are adiabatic. A sketch of the domain is shown in Figure 7, for the present configuration the lower left wall is heated with a specified heat flux. The exact solution to this domain is[12],

$$T(x,y,t) = \frac{q''W}{\lambda}(T_1 + T_2 + T_3 + T_4) + T_i \tag{15}$$

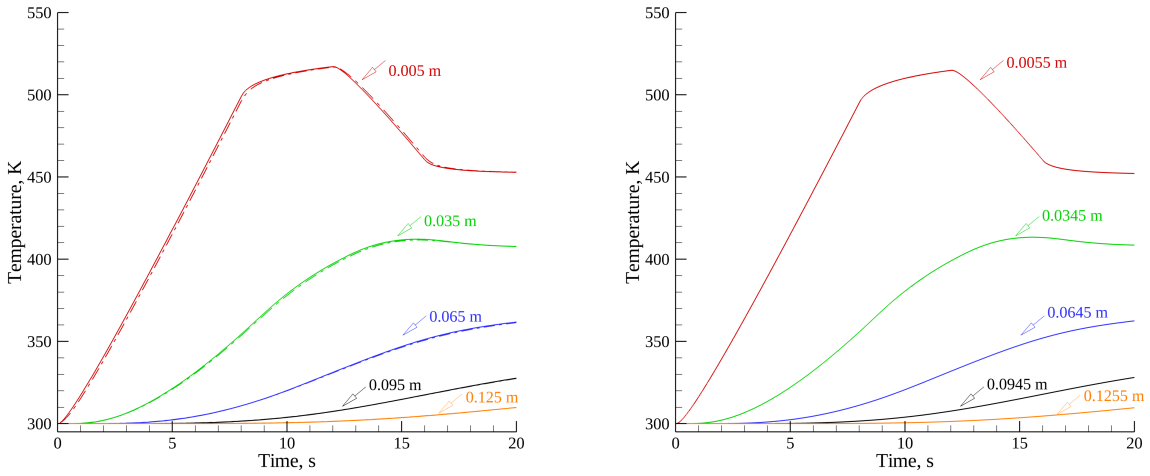

(a) $\Delta x = 0.01$ m **(b)** $\Delta x = 0.001$ m

Fig. 6 Simulation results for case 3 verification. Solid lines are simulation results and dashed lines are the exact solution.

Where,

$$T_1 = \tilde{t}_w \tilde{L}_1 \tag{16}$$

$$T_2 = \tilde{L}\left[\tilde{L}_1\tilde{t}_L + \frac{1}{12}\left(\tilde{x}_+^3 - 3\tilde{x}_+^2 + 2\tilde{x}_+ - \left(\tilde{x}_-^3 - 3\,\mathrm{sign}(\tilde{x}_-)\tilde{x}_-^2 + 2\tilde{x}_-\right)\right) - 2\sum_{m=1}^{\infty}\frac{\cos m\pi\tilde{x}\sin m\pi\tilde{L}_1}{(m\pi)^3}\exp\left(-m^2\pi^2\tilde{t}_L\right)\right] \tag{17}$$

$$T_3 = \tilde{L}_1\left[\tilde{t}_w + \frac{1}{2}\tilde{y}^2 - \tilde{y} + \frac{1}{3} - 2\sum_{n=0}^{\infty}\frac{\cos n\pi\tilde{y}}{(n\pi)^2}\exp\left(-n^2\pi^2\tilde{t}_w\right)\right] \tag{18}$$

$$T_4 = \left(\frac{1}{3} - \tilde{y} + \frac{1}{2}\tilde{y}^2\right)\frac{1 - \mathrm{sign}(\tilde{x}_-) - 2\tilde{L}_1}{2} + \sum_{n=1}^{\infty}\cos n\pi\tilde{y}\,\frac{\mathrm{sign}(\tilde{x}_-)\left(e^{-n\pi\tilde{L}|\tilde{x}_-|} - e^{-n\pi\tilde{L}(2-|\tilde{x}_-|)}\right) - e^{-n\pi\tilde{L}\tilde{x}_+} + e^{-n\pi\tilde{L}(2-\tilde{x}_+)}}{(n\pi)^2\left(1 - e^{-2n\pi\tilde{L}}\right)} - 4\sum_{m=1}^{\infty}\frac{\cos m\pi\tilde{x}\sin m\pi\tilde{L}_1}{m\pi}\sum_{n=1}^{\infty}\frac{\cos n\pi\tilde{y}}{(n\pi)^2 + (m\pi/\tilde{L})^2}\exp\left(-\pi^2(n^2 + m^2/\tilde{L}^2)\tilde{t}_w\right) \tag{19}$$

with the following non-dimensional parameters,

$$\tilde{L} = \frac{L}{W} \quad \tilde{L}_1 = \frac{L_1}{L} \quad \tilde{y} = \frac{y}{W} \quad \tilde{x} = \frac{x}{L} \quad \tilde{t}_L = \frac{t\alpha}{L^2} \quad \tilde{t}_w = \frac{t\alpha}{W^2} \quad \tilde{x}_+ = \tilde{x} + \tilde{L}_1 \quad \tilde{x}_- = \tilde{x} - \tilde{L}_1 \tag{20}$$

For the present test case, $q'' = 401 \times 10^3\ \mathrm{W\,m^{-2}}$, $L = 0.15$ m, $W = 0.04$ m, and $L_1 = 0.05$ m. Two mesh resolutions are examined, $\Delta x = \Delta y = 0.001$ m and $\Delta x = \Delta y = 0.0001$ m. These correspond to mesh sizes of 150×40 and 1500×400. The coarse mesh case was run for 2 s and the fine mesh case was run for 1 s. A representative result is shown in Figure 8. For both the coarse and fine mesh there is a slight disagreement between the solutions at the early times near the boundary. The discrepancy is eliminated at locations further away from the wall and is also eliminated near the wall later in time. Based on these four test cases, the accuracy of the solid conduction solver is determined to be adequate.

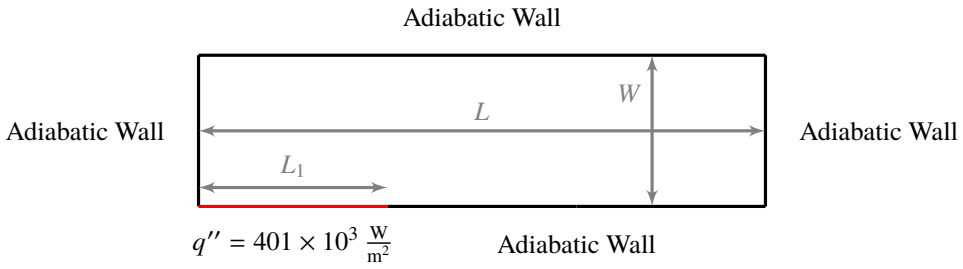

Fig. 7 Case setup for solid conduction validation case four, specified heat flux in a two-dimensional domain.

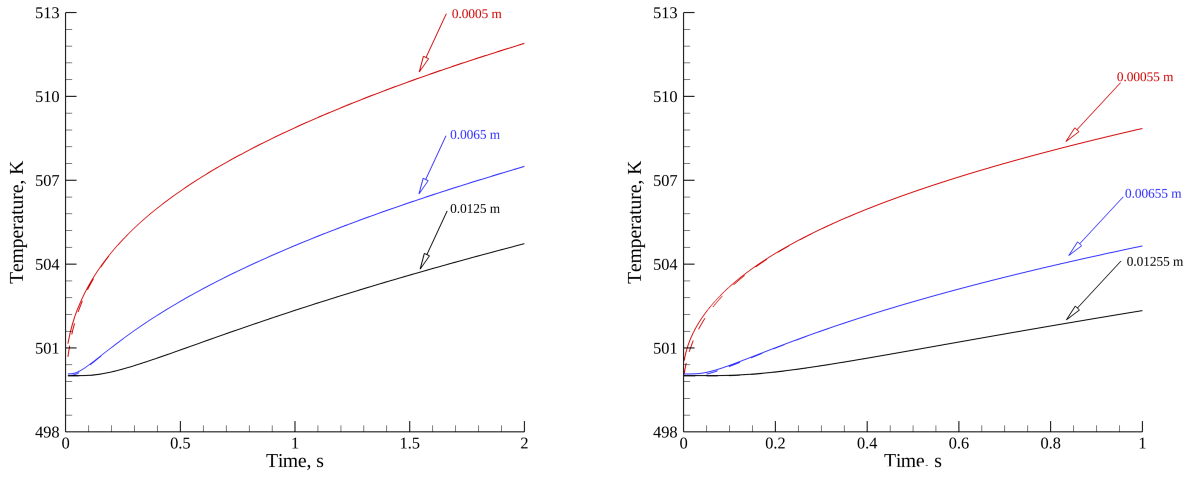

(a) $\Delta x = 0.001$ m **(b)** $\Delta x = 0.0001$ m

Fig. 8 Simulation results for case 4 verification. Solid lines are simulation results and dashed lines are the exact solution. Results shown are for $x = 0.0455$ m, and three vertical locations which are labeled.

IV. Liquid Rocket Engine Test Configuration

A. Model

To evaluate the conjugate heat transfer capability, data from a H_2-O_2 combustor are used[13]. In the experiment non-premixed hydrogen and oxygen are combusted in a 5.08 cm × 5.08 cm square combustor. The injectors are arranged in a 5 by 5 grid with a total of 25 shear coaxial injectors. The flow transitions from the combustor into a 2.54 cm × 2.54 cm test section. One side of the square test section has 6 copper plates with a width of 2.54 cm each. The copper plates are insulated from each other and instrumented individually. Downstream from the test section the flow transitions into a round nozzle with a throat diameter of 1.651 cm. The experimental configuration is shown in Figure 9 along with the computational domain. The computational investigation is completed in 2D, therefore some adjustments are made to ensure the correct area ratios. The channel height in the test section is maintained at 2.54 cm. The nozzle diameter is adjusted to 0.8428 cm to maintain the same area ratio between the test section and the nozzle throat. The inlet height is modified to 10.16 cm which maintains the area ratio between the combustor inlet section and the test section. The angle of the transition between the inlet section and test section is maintained at 14.036° by stretching the length of the transition region. A solid wall with a height of 1.27 cm is added upstream of the test section, this prevents an abrupt change in the thermal boundary condition near the test section when the boundary transitions from an adiabatic wall to the conjugate interface.

The inlet boundary is supplied with premixed products at a specified temperature, composition, and mass flow rate. The details of these parameters is given in the next section. All walls are considered to be adiabatic. The thermal penetration depth in the solid test section is small compared with the overall size of the test section which makes the adiabatic wall a reasonable assumption for the solid test section. At the outlet a mixed subsonic supersonic boundary condition is used where a fixed pressure of 101 325 Pa is used for the subsonic condition.

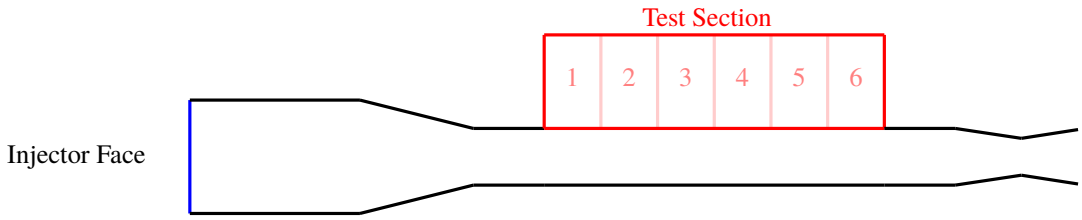

(a) Experimental setup from the injector face to the nozzle exit.

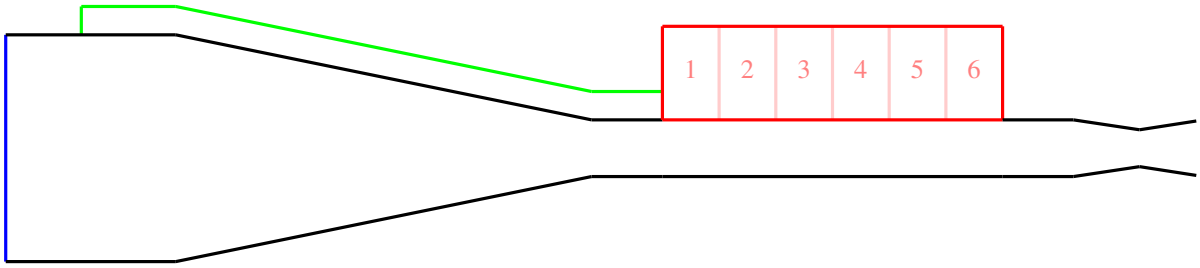

(b) Computational domain from the injector face to the nozzle exit.

Fig. 9 Case setup for solid conduction validation case four, specified heat flux in a two-dimensional domain.

A two-dimensional two-domain unstructured mesh with quadrilateral cells is used for the computation. The fluid domain contains 354,420 cells and the solid wall domain contains 282,500 cells. In the test section region of the fluid domain, a total of 180 cells are used in the vertical direction with a first cell height of 0.127 µm. A total of 900 cells is used in the horizontal direction of the test section with a uniform spacing of 0.1693 mm. In the solid wall section of the fluid domain 100 cells are used in the first 1.27 cm with a uniform spacing of 0.127 mm, some grid stretching is used outside of this region to reduce the cost. The code is run with the k-ω turbulence model[14]. A H_2-O_2 finite rate combustion model is used which contains 8 species and 25 reactions based on the FFCM-1 model with reactions including carbon omitted[15, 16]. A fixed time step of 1 µs is used for the solver and information at the solid-fluid interface is exchanged at each time step. Simulations are run for 0.1 s which is sufficient for the entire test section surface temperature to exceed the targeted experimental surface temperature.

Table 1 Operating Conditions.

Property	Condition 1	Condition 2	Condition 3	Condition 4
O_2 Flow Rate, lbm/s	0.14823	0.40835	0.50857	0.63937
H_2 Flow Rate, lbm/s	0.02624	0.06898	0.09082	0.11604
O/F Ratio	5.649	5.920	5.560	5.510
Total Flow Rate, kg/s	0.07914	0.21651	0.27188	0.34265
2D Flow Rate, kg/s	3.1157	8.5241	10.7039	13.4901
Pressure, psia	107	310	415	522
Pressure, MPa	0.7377	2.1374	2.8613	3.5991
Temperature, K	3267	3429	3431	3446
O_2 Mass Fraction	0.01550	0.01605	0.00977	0.00794
H_2 Mass Fraction	0.04592	0.04037	0.04657	0.04848
H Mass Fraction	0.00536	0.00430	0.00408	0.00386
O Mass Fraction	0.00969	0.00883	0.00609	0.00511
OH Mass Fraction	0.08018	0.08101	0.06793	0.06278
H_2O Mass Fraction	0.84332	0.84933	0.86549	0.87175
HO_2 Mass Fraction	0.00005	0.00009	0.00006	0.00006
H_2O_2 Mass Fraction	0.00001	0.00002	0.00001	0.00002

B. Operating Conditions

Simulations for four different operating conditions were completed to determine the ability of the model to predict the wall heat flux. To simplify the model the 25 injectors are replaced with a constant mass flow rate at a temperature and composition consistent with complete combustion. The NASA CEA tool is used to obtain the inlet conditions[17]. This assumption is reasonable because the experimental hardware was designed to supply the test section with fully combusted uniform flow. The two-dimensional simulations require that the mass flow rate for the computation be scaled by a factor of 0.0254^{-1}. This scaling is required to properly account for the difference in scaling lengths and areas in the conversion from the three-dimensional geometry to the two-dimensional geometry. The result of the scaling is a matching of velocities between the computation and experiment. The operating conditions for each of the four simulations conducted are summarized in Table 1. The primary variation between the four conditions is increasing chamber pressure. There is also some variation in the O/F ratio, with condition 2 having a larger O/F ratio than the other three cases.

C. Results

1. Flowfield

Figure 10 shows the temperature contour after 0.1 s for the entire flowfield as well as a zoomed-in region near the start of the test section. Comparing the upper wall, which has the conjugate interface, and the lower wall, which has the adiabatic boundary condition, you can see differences in the flowfield temperature. The temperature adjacent to the upper wall is lower than the core temperature. Inside the solid wall the temperature remains close to the initial starting temperature of 350 K for most of the domain. The zoomed-in view of the test section has a restricted contour level to better show the temperature variation in the solid. At the start of the test section, you can see the temperature is above 350 K adjacent to the fluid wall but still much lower than the fluid temperature. The region of elevated temperature is restricted to just the first 1.27×10^{-2} m into the solid. As you move downstream in the section the penetration depth of the thermal conduction decreases along with the surface temperature. Beyond the test section, where the boundary condition transitions from the conjugate interface to the adiabatic wall, the temperature rapidly increases. Both plots show that the temperature of the fluid is largely constant except for the near wall region adjacent to the solid-fluid interface.

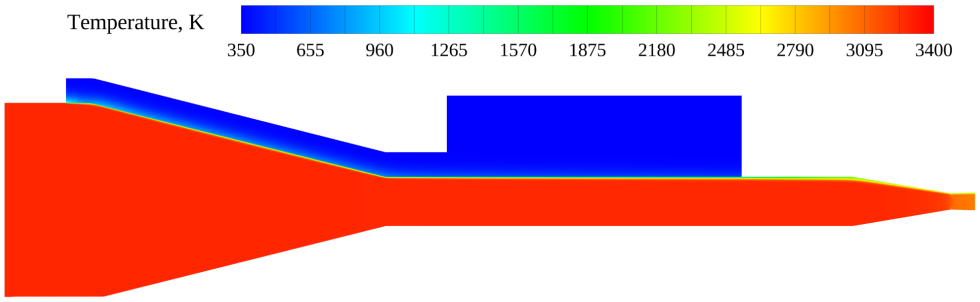

(a) Full view.

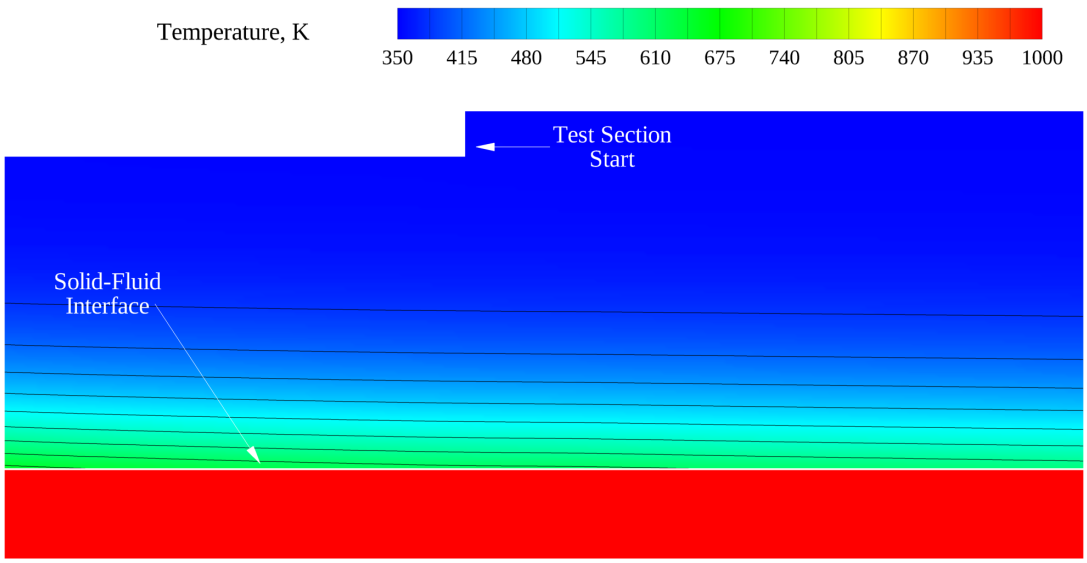

(b) Zoomed view at the start of the test section.

Fig. 10 Temperature contour for condition one. The top plot shows the full combustor, it is difficult to see the impact of the heating in the test section in this view. The lower view shows a zoomed in plot at the start of the test section. In the constrained view the temperature of fluid is clipped at 1000 K to better show the thermal penetration in the solid.

2. Profiles

Figure 11 shows the temperature profile 1 cm from the start of the test section and 5 cm from the start of the test section (1 cm from the end). These two locations represent the starting and ending points of the region that was used for the experimental calculation of the heat flux. The figure shows two views, a standard view and a zoomed-in view near the solid-fluid interface. For each of the plots, four solution times are plotted. You can see that the interface temperature increases as the simulation run time increases. At the 1 cm location there is a small difference in the temperature on the fluid side between the 0.075 s time and 0.100 s time. On the solid side, the temperature is still changing between 0.075 s and 0.100 s. The majority of the copper test section remains close to the initial temperature, 350 K, for the entire simulation. Comparing the profiles between the 1 cm and 5 cm location shows a thickening of the thermal boundary layer near the wall as you move downstream in the test section. The thermal gradient near the wall also decreases as you move downstream in the test section; this is consistent with the wall heat flux which decreases as you move downstream.

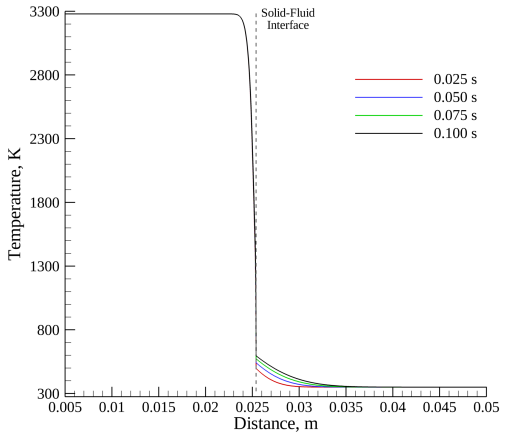

(a) Wide view, 1 cm**.**

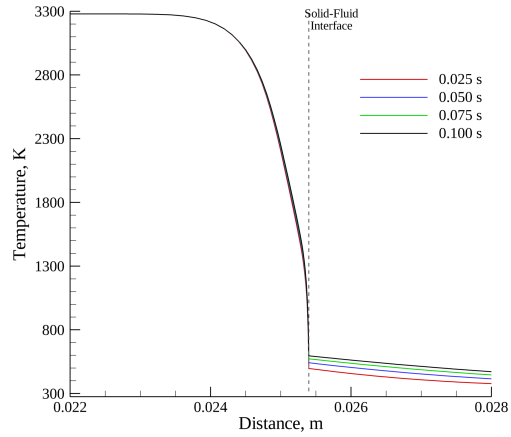

(b) Zoomed view, 1 cm**.**

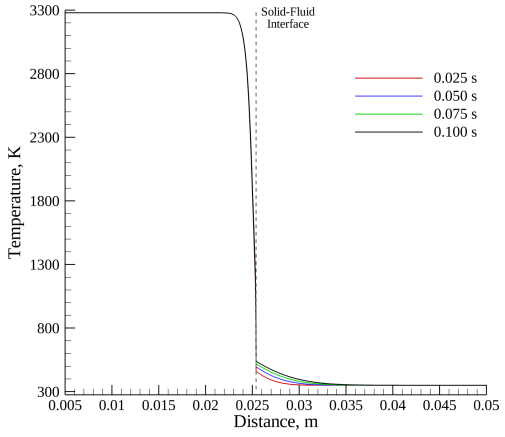

(c) Wide view, 5 cm**.**

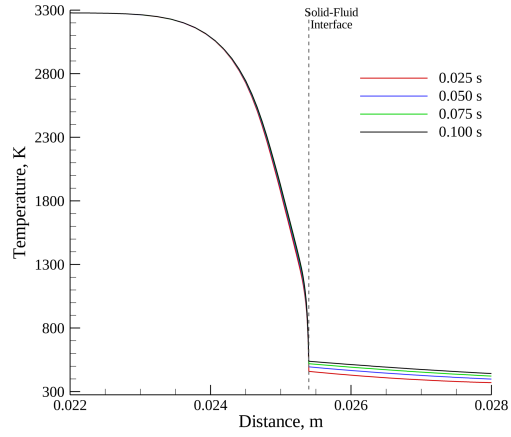

(d) Zoomed view, 5 cm**.**

Fig. 11 Temperature profile near the solid-fluid interface in the test section. 1 cm **is the start of the experimental averaging section and** 5 cm **is the end of the experimental averaging section.**

Figure 12 shows four species mass fraction profiles in the near wall region for conditions one and four. H_2O, OH, O_2, and H_2 are plotted at the 1 cm location and the 5 cm location. Conditions one and four have different free stream compositions but the profiles are similar. Like the temperature contour, the composition only changes in the near wall region as a result of a new equilibrium composition at the lower temperature. There is a thickening of the species

boundary layer as you move downstream which is more pronounced at the lower pressure (condition one) operating point. In each plot there is an increase in water vapor near the wall and a reduction in OH and O_2. The H_2 mass fraction is largely constant with a slight dip as you approach the solid-fluid interface.

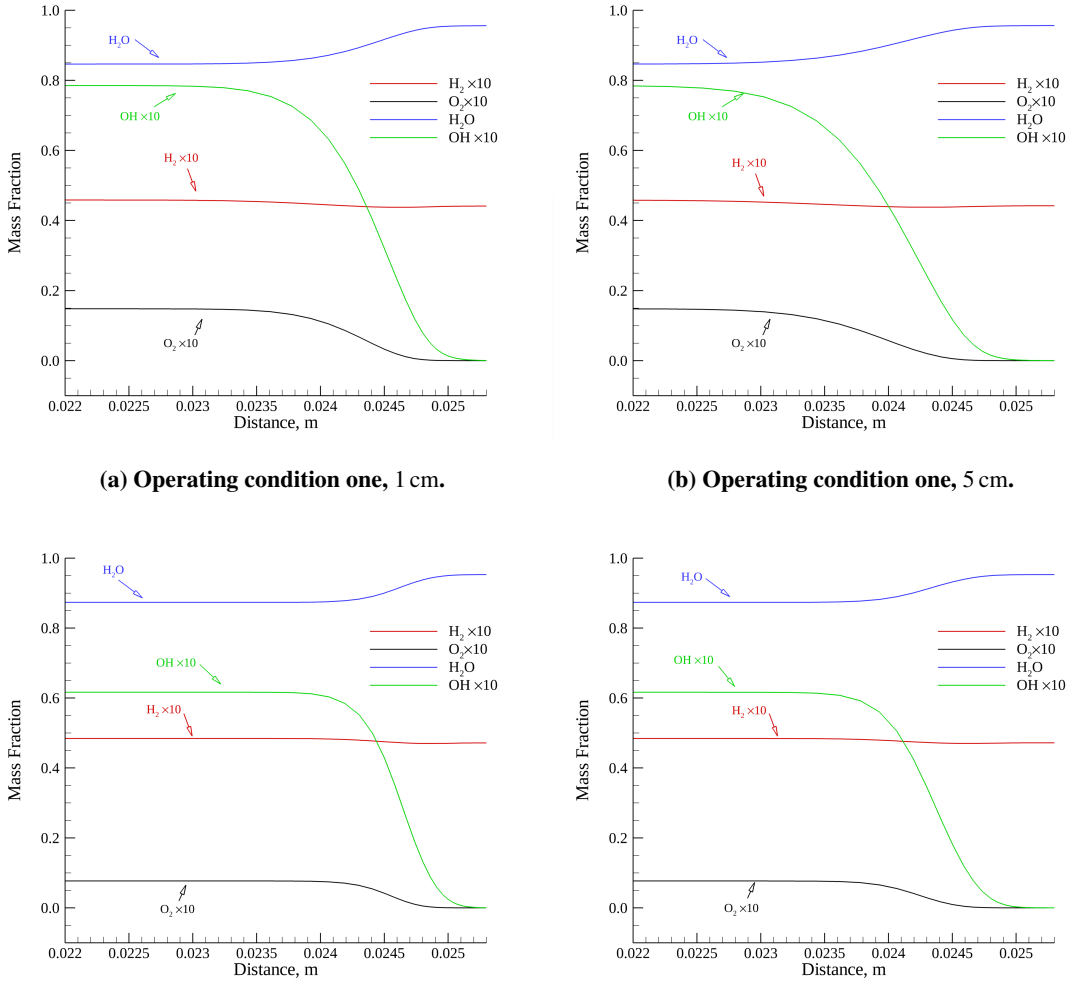

(a) Operating condition one, 1 cm**.**

(b) Operating condition one, 5 cm**.**

(c) Operating condition four, 1 cm**.**

(d) Operating condition four, 5 cm**.**

Fig. 12 Selected species profiles near the solid-fluid interface in the test section for operating conditions one and four. 1 cm **is the start of the experimental averaging section and** 5 cm **is the end of the experimental averaging section. H_2, O_2, and OH mass fractions are scaled by a factor of ten.**

To better understand the effect of changing species mass fraction on the heat transfer the thermal conductivity is examined. Figure 13 shows the thermal conductivity in the near wall region for condition four. Similar to the temperature profile the thermal conductivity decreases near the wall compared with the free stream conductivity. Also included in the figure is the thermal conductivity calculated with frozen chemistry. The thermal conductivity with frozen composition decreases, but not to the same extent as the reacting flow calculation. The decreasing thermal conductivity is a result of the change in the temperature and the resulting change in the equilibrium composition near the conjugate interface. This illustrates the importance that chemical kinetics be included in the simulation to correctly capture changes in the composition and the resulting thermal conductivity.

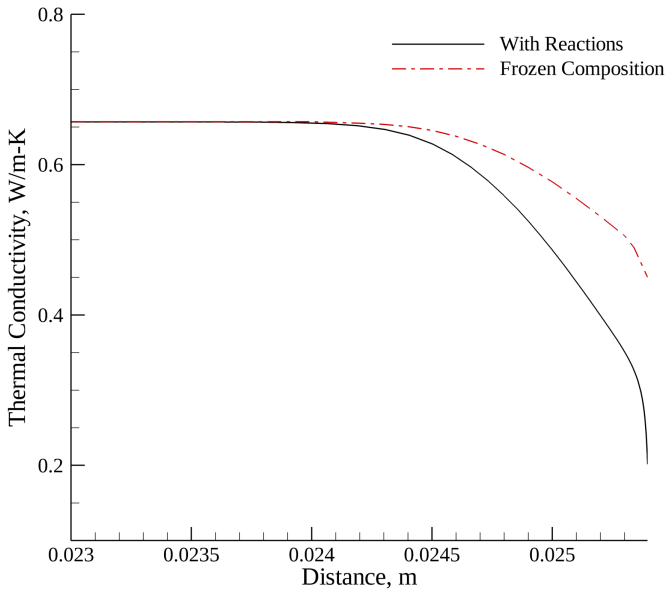

Fig. 13 Thermal conductivity of the fluid near the wall for condition four at the 1 cm location. The conductivity is shown for the reacting flow case and for the case when the composition is frozen.

3. Heat Flux

The key metric for comparison with the experimental results is the heat flux. The experimental heat flux was computed at a surface temperature which was different for each of the four operating conditions. The reported experimental data is the average heat flux in test sections 2 through 5 once the targeted surface temperature was reached[13]. The simulations use a similar data reduction procedure where the heat flux is averaged in test sections 2 through 5 any time the surface temperature is within the specified temperature plus a tolerance of ±0.1 K. Results were found to be insensitive to the tolerance used. Larger tolerances of ±0.25 K and ±0.5 K generated more matching data but resulted in the same average heat flux. Experimental and computed heat fluxes are shown in Table 2. The results show excellent agreement for conditions 1, 3, and 4. The error in each of these cases is within 4% of the experimental data. The heat flux for condition 2 is larger than the experimental heat flux and has an error of almost 10%. A view of the spatial variation in heat flux over the entire test section is shown in Figure 14. The plot shows the heat flux when the surface temperature reaches the prescribed surface temperature (Table 2), these data points are not necessarily occurring at the same physical time in the simulation since the test section is not heated uniformly. At the head end of the test section, the heat flux is considerably higher than at the trailing edge. This is consistent with the temperature gradient observations, in the downstream section of the test section the thermal boundary layer has had time to thicken. A result of this thickening is a decrease in the temperature gradient adjacent to the wall. Condition two and four, the conditions with larger error, show increased variability in the heat flux while the other two conditions exhibit a smooth curve along the length of the test section.

For condition two, it is not clear what behaves differently that results in the higher error. We note that case 2 did have a larger O/F ratio than the other three cases but have not correlated this to the difference in behavior at this time. The initial composition and temperature used are largely similar to the other three conditions. The operating point for condition two is not an outlier, the pressure and mass flow rate are in between conditions one and three. One notable difference is that the surface temperature used to define the heat flux, 459.26 K, was the lowest of the four conditions. It is possible that with the low surface temperature the system is still in an initial transient and the simulation may not able to accurately capture this initial transient period due to approximations or a sensitivity to the initial conditions. It is also possible that there is additional experimental uncertainty at the lower surface temperature because the system is still in a rapidly changing thermal environment. To investigate the effect of surface temperature on the computed average heat flux condition two was reexamined at three additional surface temperatures. The data for this is tabulated in Table 3. At

Table 2 Average heat flux results for the computation and experiment. The reported data is the average heat flux when the surface reaches specified surface temperature. In each case only the data from test sections 2 through 5 are used in the average.

Simulation	Surface Temperature, K	Experimental Heat Flux, btu/in^2-s	Computational Heat Flux, btu/in^2-s	Error
Condition 1	481.48	2.8	2.782	0.64%
Condition 2	459.26	6.6	7.238	9.67%
Condition 3	549.82	8.3	8.082	2.63%
Condition 4	545.37	10.1	10.487	3.83%

the higher surface temperature, the predicted heat flux decreases and approaches the experimental value. This data suggests that either the experimental data is inaccurate, or that the computations are unable to predict the heat flux for this startup transient period.

4. Grid Resolution

To investigate potential cost savings and better understand the resolution requirements, the near wall grid resolution was examined. In this series of simulations, the first cell height was adjusted to be a factor of two larger than the baseline condition, ($\Delta x = 5.08 \times 10^{-7}$ m). The grids were otherwise the same, the heat flux results for these simulations are shown in Table 4. For condition 1 the heat flux result is reasonable, the error increased from 0.64% to 4.68%, which may still be acceptable for design simulations. The results for the other three conditions are no longer acceptable. Condition two remains the outlier with an error greater than a factor of two. Conditions three and four have an error that is more than ten times larger than the fine grid simulation. While this coarse grid can reproduce the trend of heat flux with chamber pressure, the results show that care must be taken to properly resolving the near-wall region to accurately predict the heat flux.

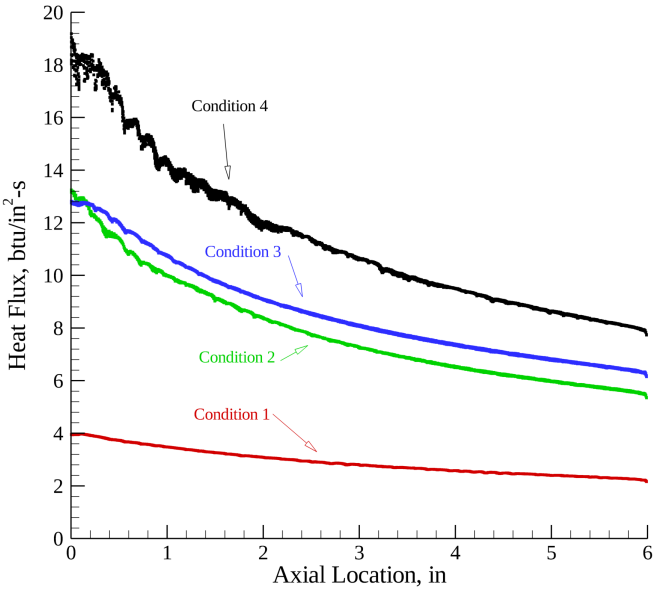

Fig. 14 Computed heat flux for each of the four operating conditions as a function of position in the test section. Note that not all data points occur at the same instance in time.

Table 3 Average heat flux results for condition two with a varied surface temperature. The reported data is the average heat flux when the surface reaches specified surface temperature. In each case only the data from test sections 2 through 5 are used in the average. The surface temperature in the experiment is reported as 459.26 K**.**

Surface Temperature	Heat Flux, btu/in^2-s	Error
Experiment	6.6	—
459.26 K	7.238	9.67%
480.00 K	6.956	5.39%
500.00 K	6.774	2.64%
520.00 K	6.650	0.76%

Table 4 Average heat flux results for the coarse grid computation and experiment. The reported data is the average heat flux when the surface reaches specified surface temperature. In each case only the data from test sections 2 through 5 are used in the average.

Simulation	Surface Temperature, K	Experimental Heat Flux, btu/in^2-s	Computational Heat Flux, btu/in^2-s	Error
Condition 1	481.48	2.8	2.931	4.68%
Condition 2	459.26	6.6	15.3826	133.07%
Condition 3	549.82	8.3	11.0622	33.28%
Condition 4	545.37	10.1	13.7453	36.09%

V. Summary and Future Work

In this work, a conjugate heat transfer capability was developed to evaluate the wall heat flux in a liquid rocket combustor. The tool's ability to accurately solve the solid conduction in the wall was validated through a series of four exact solutions. To evaluate the conjugate heat transfer capability a H_2-O_2 liquid rocket engine experiment was simulated. The average heat flux was computed in a copper-walled test section attached to the combustor. The experiment and simulation were run for four different chamber pressures, as the chamber pressure increased so did the heat flux. The simulations were able to accurately predict this trend in heat flux as well as the magnitude of the heat flux within 4% for three of the four chamber pressures. The middle chamber pressure was an outlier which may be related to the low surface temperature that was used to compute the heat flux. Simulations showed that the species composition changed in the near wall region as the flow reached a new equilibrium state at a lower temperature. Both the change in composition and temperature must be captured to accurately predict the local thermal conductivity of the fluid. A grid resolution study showed that an extremely fine mesh is required to predict the heat flux. In the future the conjugate model will be paired with a wall model to reduce the cost of the simulations.

VI. Acknowledgments

Computing resources were provided by the DoD High Performance Computing Modernization Program (HPCMP).

References

[1] Moroz, L., Burlaka, M., Barannik, V., Kochurov, R., and Maksiuta, D., "Liquid Rocket Propulsion Launcher Design System to Train AxSTREAM. AI. Reusability Aspects." *8th European conference for aeronautics and space sciences (EUCASS)*, 2019, pp. 1–11.

[2] Jiawen, S., and Bing, S., "Thermal-structural analysis of regeneratively-cooled thrust chamber wall in reusable LOX/Methane rocket engines," *Chinese Journal of Aeronautics*, Vol. 30, No. 3, 2017, pp. 1043–1053.

[3] Oschwald, M., Suslov, D., Haemisch, J., Haidn, O., Celano, M., Kirchberger, C., Rackemann, N., Preuss, A., and Wiedmann, D., "Measurement of heat transfer in liquid rocket combustors," , 2020.

[4] Perakis, N., Strauß, J., and Haidn, O. J., "Heat flux evaluation in a multi-element CH4/O2 rocket combustor using an inverse heat transfer method," *International Journal of Heat and Mass Transfer*, Vol. 142, 2019, p. 118425.

[5] Harvazinski, M. E., Huang, C., Sankaran, V., Feldman, T. W., Anderson, W. E., Merkle, C. L., and Talley, D. G., "Coupling between hydrodynamics, acoustics, and heat release in a self-excited unstable combustor," *Physics of Fluids*, Vol. 27, No. 4, 2015, p. 045102.

[6] Lian, C., Xia, G., and Merkle, C. L., "Solution-limited time stepping to enhance reliability in CFD applications," *Journal of Computational Physics*, Vol. 228, No. 13, 2009, pp. 4836–4857.

[7] Li, D., Xia, G., Sankaran, V., and Merkle, C., "Computational Framework for Complex Fluids Applications," *3rd International Conference on Computational Fluid Dynamics*, Toronto, Canada, 2004, pp. 619 – 624.

[8] Xia, G., Sankaran, V., Li, D., and Merkle, C., "Modeling of Turbulent Mixing Layer Dynamics in Ultra-High Pressure Flows," *36th AIAA Fluid Dynamics Conference and Exhibit*, San Francisco, CA, 2006, pp. 1–17. AIAA Paper 2006-3729.

[9] Lian, C., Xia, G., and Merkle, C., "Impact of Source Terms on Reliability of CFD Algorithms," *Computers and Fluids*, Vol. 39, 2010, pp. 1909–1922.

[10] Incropera, F., Dewitt, D., Bergman, T., and Lavine, A., *Fundamentals of Heat and Mass Transfer*, sixth ed., Wiley, Hoboken, NJ, 2007.

[11] Carslaw, H., and Jaeger, J., *Conduction of heat in solids*, 2nd ed., Oxford University Press, New York, 1959.

[12] Woodbury, K. A., Najafi, H., and Beck, J. V., "Exact analytical solution for 2-D transient heat conduction in a rectangle with partial heating on one edge," *International Journal of Thermal Sciences*, Vol. 112, 2017, pp. 252–262.

[13] Coy, E. B., and Danczyz, S. A., "Measurements of the effectiveness of concave spherical dimples for enhancement heat transfer," *Journal of Propulsion and Power*, Vol. 27, No. 5, 2011, pp. 955–958.

[14] Wilcox, D. C., "Formulation of the k-ω turbulence model revisited," *AIAA journal*, Vol. 46, No. 11, 2008, pp. 2823–2838.

[15] "Foundational Fuel Chemistry Model Version 1.0 (FFCM-1)," http://nanoenergy.stanford.edu/ffcm1, 2016.

[16] Tao, Y., Smith, G. P., and Wang, H., "Critical kinetic uncertainties in modeling hydrogen/carbon monoxide, methane, methanol, formaldehyde, and ethylene combustion," *Combustion and Flame*, Vol. 195, 2018, pp. 18–29.

[17] Gordon, S., and McBride, B. J., "Computer Program for Calculation of Complex Chemical Equilibrium," *NASA reference publication*, Vol. 1311, 1994.

U.S. AIR FORCE

USSF

AFRL

Conjugate Heat Transfer Analysis of the Wall Heat Flux in a Liquid Rocket Engine

Matthew Harvazinski[1] and Tomas Houba[2]

1 – Air Force Research Laboratory

2 – SLI Inc.

Edwards AFB, CA

Outline

- Motivation
- Verification of Solid Conduction Modeling
- Development of a Conjugate Heat Transfer Solver
- Results for a Liquid Rocket Engine Test Article
- Summary and Future Work

Motivation

- Thermal management in liquid rocket engines is a key design challenge
- The heat transfer from the combustor to the walls and injector face are a function of the runtime, operating conditions, and can have significant spatial variations
- Prediction of the wall heat flux and wall temperature is challenge for computational tools
  - Resolution of thermal gradients is expensive
  - Adiabatic wall boundary conditions are frequently used, these cannot be used to predict the wall temperature of heat flux
- Accurate prediction of the wall temperature and heat flux requires knowledge of the fluid domain and solid wall domain
- Goal:

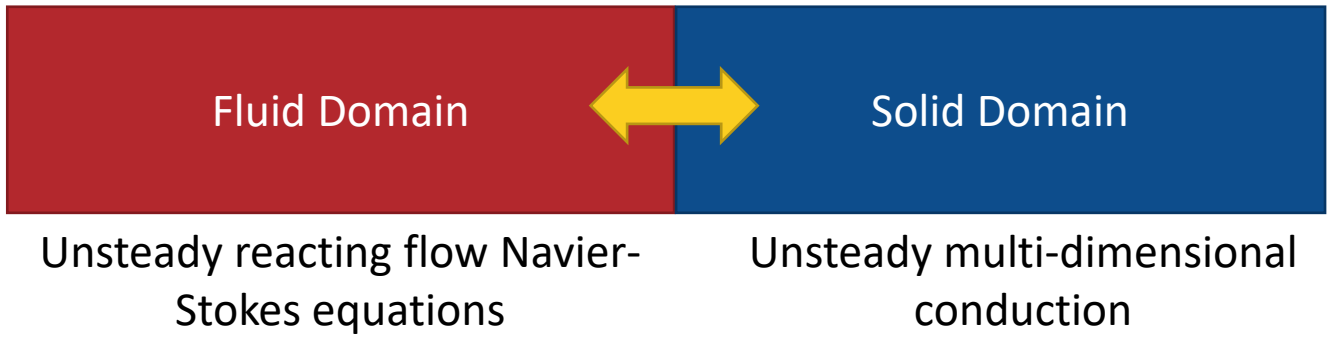

Verification of Solid Conduction

- Capability built in the in-house GEMS code. This code already solves the unsteady reacting flow Navier-Stokes equations.
- Looking at the energy equation:

$$\rho\frac{\mathrm{D}h^0}{\mathrm{D}t} = \frac{\partial p}{\partial t} - \frac{\partial}{\partial x_i}\left(-\lambda\frac{\partial T}{\partial x_i} + \rho\sum_{k=1}^{N} h_k Y_k V_{k,i}\right) + \frac{\partial}{\partial x_j}\left(\tau_{ij}u_i\right)$$

- This is valid inside the solid; we can make a number of simplifications, no variation in pressure, zero velocity, no multi-species effects, that reduces the equation to:

$$\rho\frac{\partial h^0}{\partial t} = \frac{\partial}{\partial x_i}\left(\lambda\frac{\partial T}{\partial x_i}\right)$$

- For the present work we use a constant properties equation of state where density, thermal conductivity and specific heat are constant, this yields:

$$h^0 = c_p T \qquad \alpha = \frac{\lambda}{\rho c_p}$$

$$\boxed{\frac{\partial T}{\partial t} = \alpha\frac{\partial^2 T}{\partial x_i^2}}$$

Test Case 4 – 2D Conduction in a Solid Slab

A constant heat flux is applied to a portion of one wall with the other walls adiabatic.

The exact solution is:

$$T(x,y,t) = \frac{q''W}{\lambda}\left(T_1 + T_2 + T_3 + T_4\right) + T_i$$

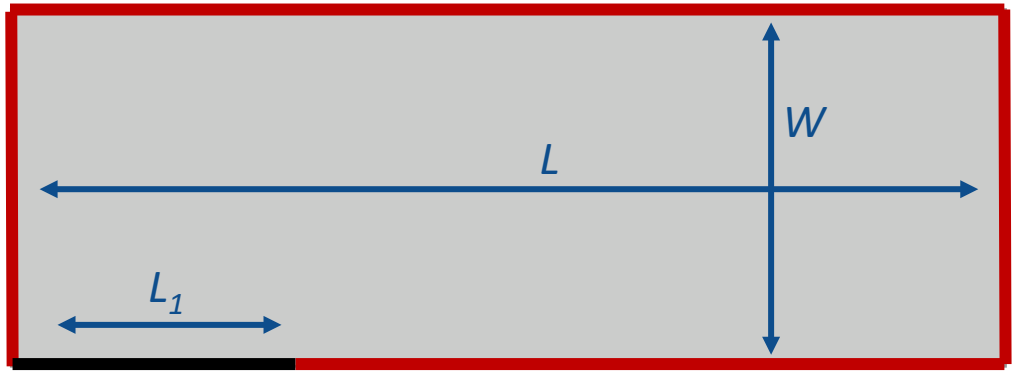

Where T_1, T_2, T_3, and T_4 are functions of time and position. For example:

$$T_2 = \tilde{L}\left[\tilde{L}_1\tilde{t}_L + \frac{1}{12}\left(\tilde{x}_+^3 - 3\tilde{x}_+^2 + 2\tilde{x}_+ - \left(\tilde{x}_-^3 - 3\,\mathrm{sign}(\tilde{x}_-)\tilde{x}_-^2 + 2\tilde{x}_-\right)\right) - 2\sum_{m=1}^{\infty}\frac{\cos m\pi\tilde{x}\sin m\pi\tilde{L}_1}{(m\pi)^3}\exp\left(-m^2\pi^2\tilde{t}_L\right)\right]$$

Test Case 4 – 2D Conduction in a Solid Slab

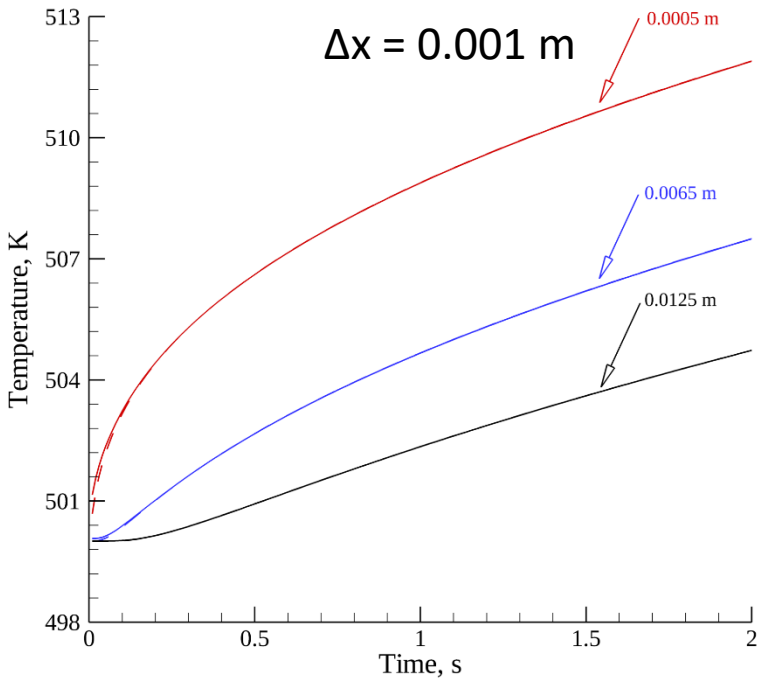

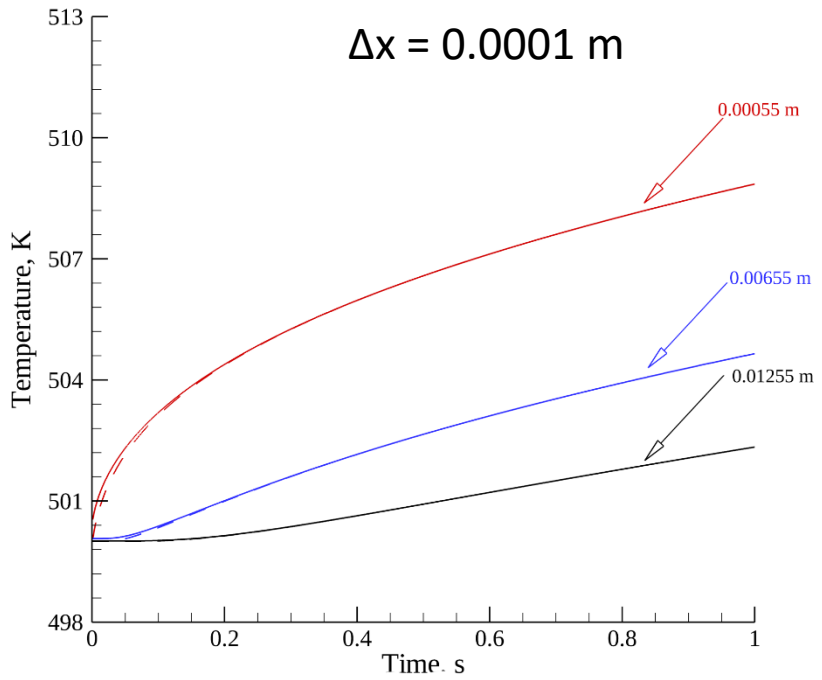

- Both resolutions show minor difference between the exact solution and computation close to the boundary at early times.
- Some of this error may be related to truncation errors in the exact solution which relies on the cancelation of terms with large values at early times

Development of a Conjugate Solver

- On the fluid side the no slip boundary condition is enforced
- The interface temperature is applied as a boundary condition to each domain.
- The interface temperature is computed using one-sided differences at the interface:

$$\lambda_f \frac{T_f - T_w}{d_f} = \lambda_s \frac{T_w - T_s}{d_s}$$

- Solving for the wall temperature yields:

$$T_w = \frac{\frac{\lambda_f}{d_f} T_f + \frac{\lambda_s}{d_s} T_s}{\frac{\lambda_f}{d_f} + \frac{\lambda_s}{d_s}}$$

- And we can compute the heat flux:

$$q''_w = \lambda_s \frac{T_w - T_s}{d_s}$$

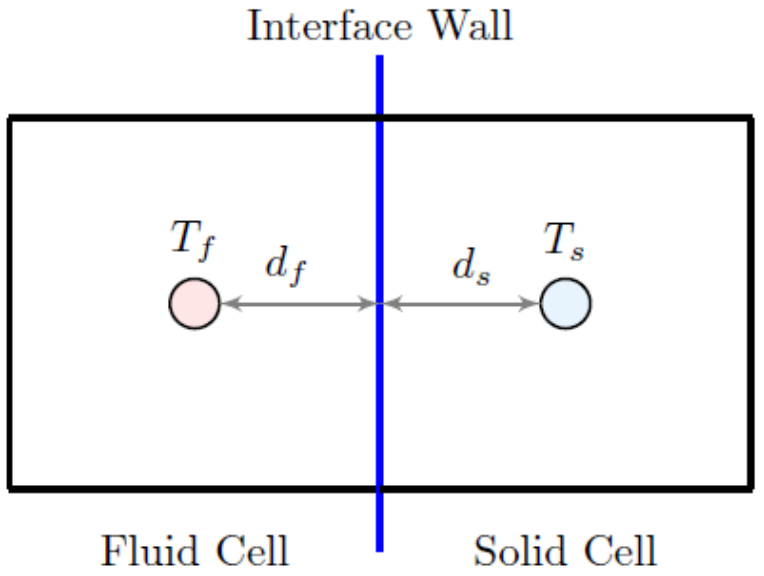

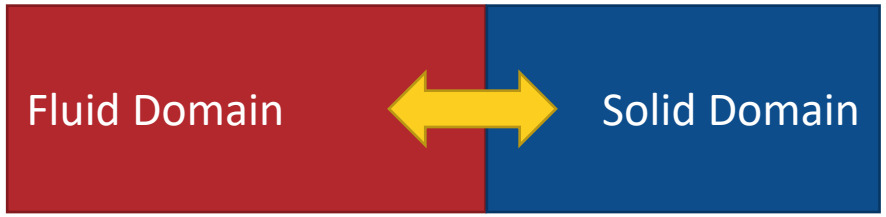

Liquid Rocket Engine Test Case

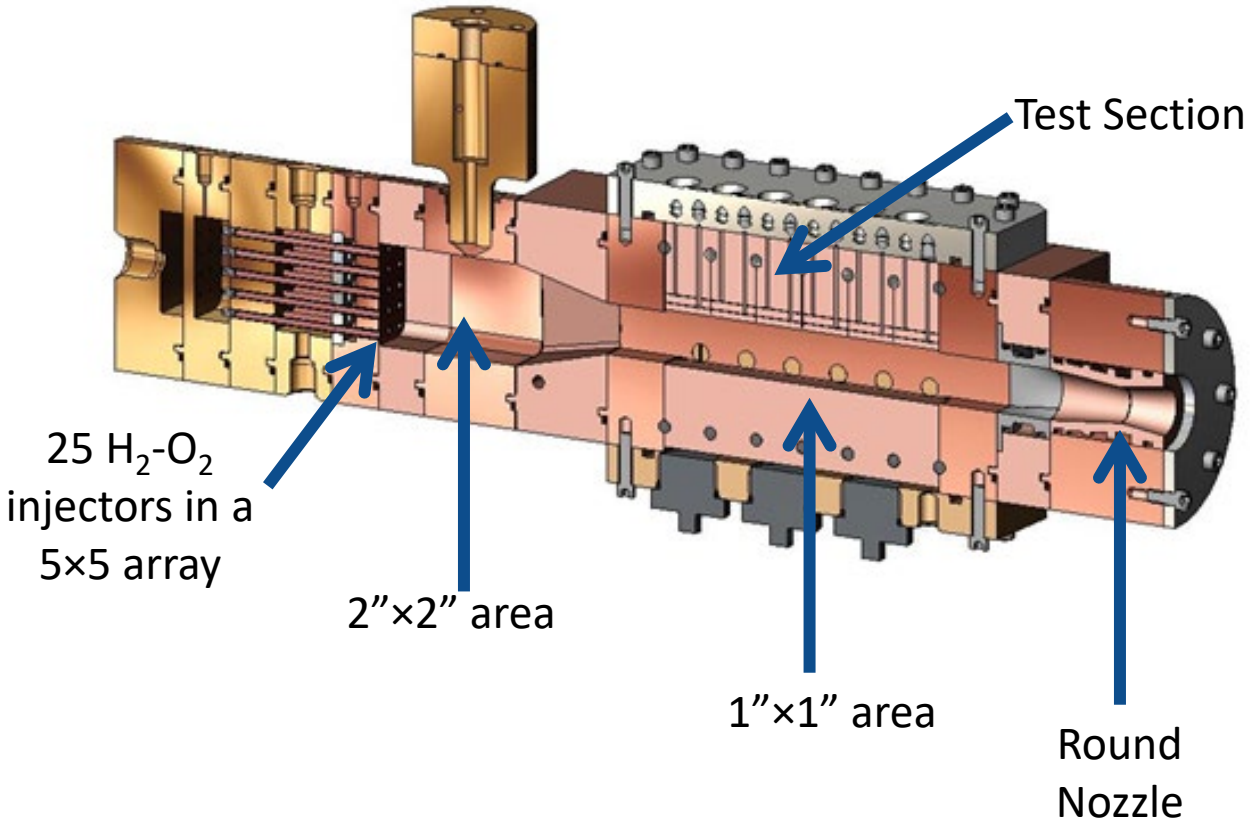

- The test section consists of 6 1” long insulated copper bars
- The heat flux and surface temperature are measured in each of the bars
- The reported experimental heat flux is the average heat flux in bars 2-4, the first and last are excluded

Liquid Rocket Engine Test Case – Computational Setup

- The simulation is run in 2D, which requires some adjustments
  - The test section area is maintained
  - The combustor inlet is modified to maintain the correct area ratio between the combustor and the test section, the transition region is elongated to maintain the same angle
  - The nozzle throat area is adjusted to maintain the same area ratio between the test section and the throat
  - The 25 injectors are replaced with a uniform mass flow of combusted products.

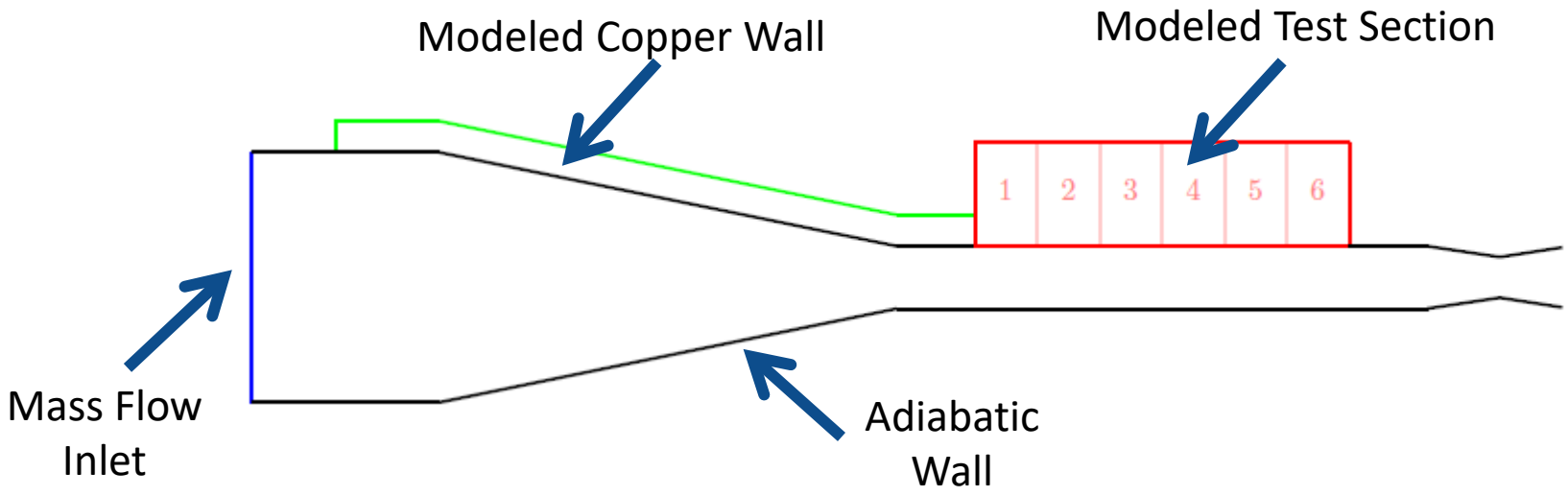

- Fluid domain – 354420 cells
- Solid domain – 282500 cells
- Fluid first cell height, 0.0127µm
- 8 species 25 reaction H_2/O_2 finite rate kinetics model
- 0.2 second run time with a fixed timestep of 1×10^{-6} s

Operating Conditions

Property	Condition 1	Condition 2	Condition 3	Condition 4
O_2 Flow Rate, lbm/s	0.14823	0.40835	0.50857	0.63937
H_2 Flow Rate, lbm/s	0.02624	0.06898	0.09082	0.11604
O/F Ratio	5.649	5.920	5.560	5.510
Total Flow Rate, kg/s	0.07914	0.21651	0.27188	0.34265
Computational Flow Rate, kg/s	3.1157	8.5241	10.7039	13.4901
Pressure, psia	107	310	415	522
Pressure, MPa	0.7377	2.1374	2.8613	3.5991
Temperature, K	3267	3429	3431	3446
O_2 Mass Fraction	0.01550	0.01605	0.00977	0.00794
H_2 Mass Fraction	0.04592	0.04037	0.04657	0.04848
H Mass Fraction	0.00536	0.00430	0.00408	0.00386
O Mass Fraction	0.00969	0.00883	0.00609	0.00511
OH Mass Fraction	0.08018	0.08101	0.06793	0.06278
H_2O Mass Fraction	0.84332	0.84933	0.86549	0.87175
HO_2 Mass Fraction	0.00005	0.00009	0.00006	0.00006
H_2O_2 Mass Fraction	0.00001	0.00002	0.00001	0.00002

Computed Heat Flux

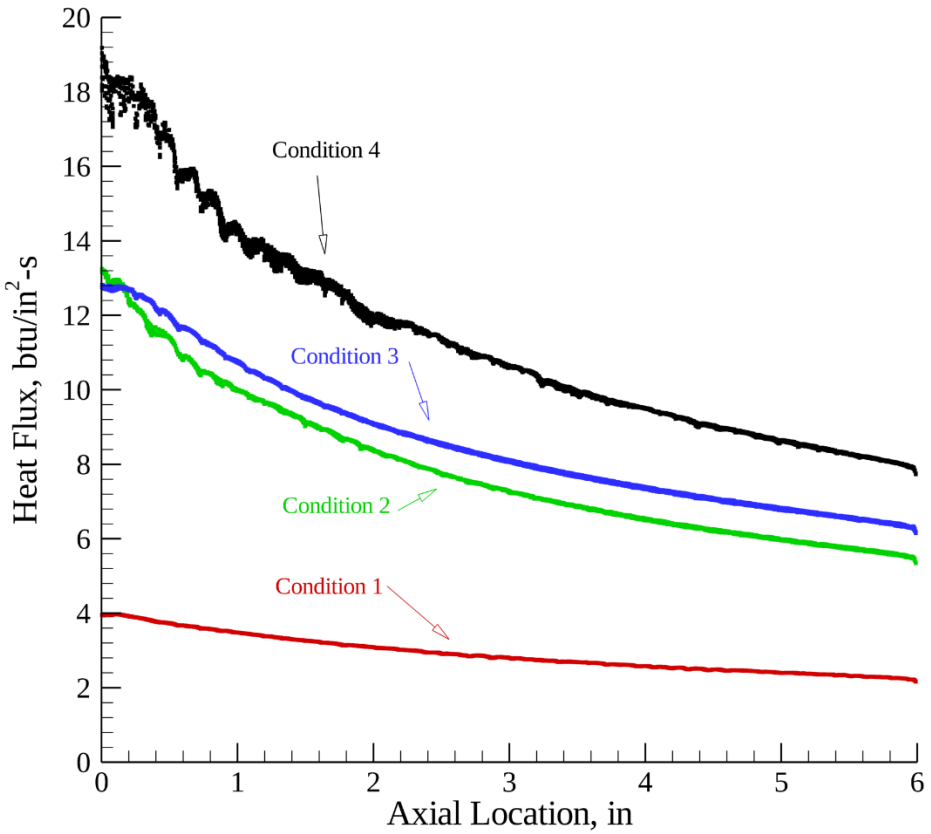

Cond.	Surface Temp, K	Exp. Heat Flux, btu/in²-s	Comp. Heat Flux, btu/in²-s	Error
1	481.48	2.8	2.782	0.64%
2	459.26	6.6	7.238	9.67%
3	549.82	8.3	8.082	2.63%
4	545.37	10.1	10.487	3.83%

- Excellent agreement for cases 1, 3, and 4
- What is different about case 2?
  - Larger O/F ratio
  - Lower surface temperature

Condition 1 Flowfield

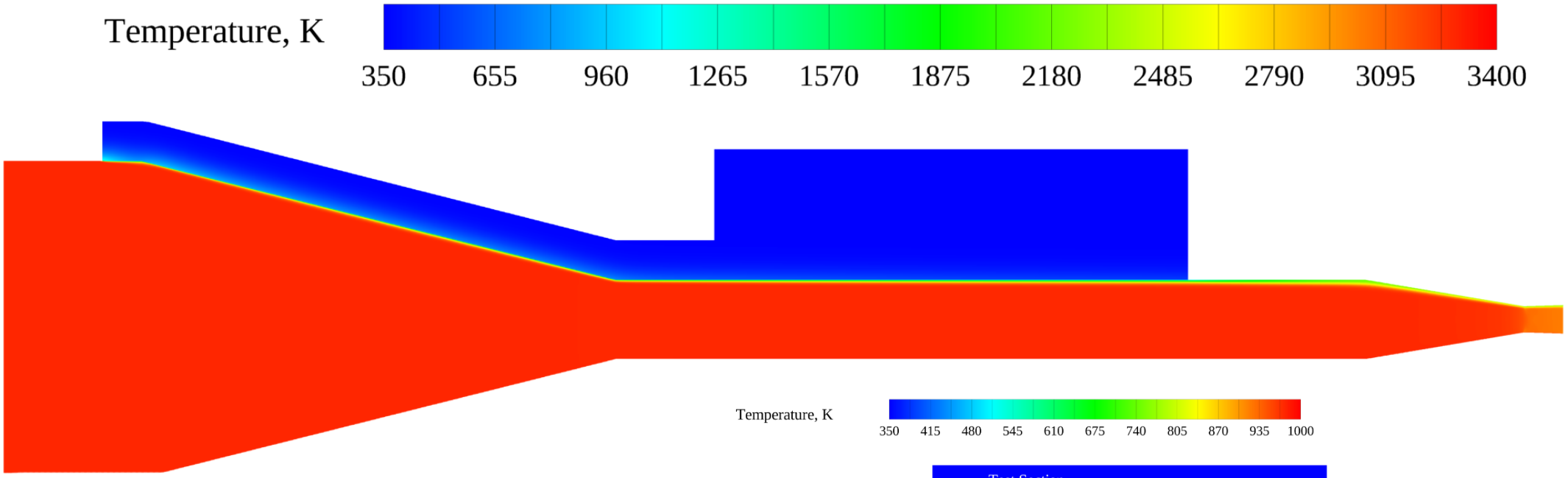

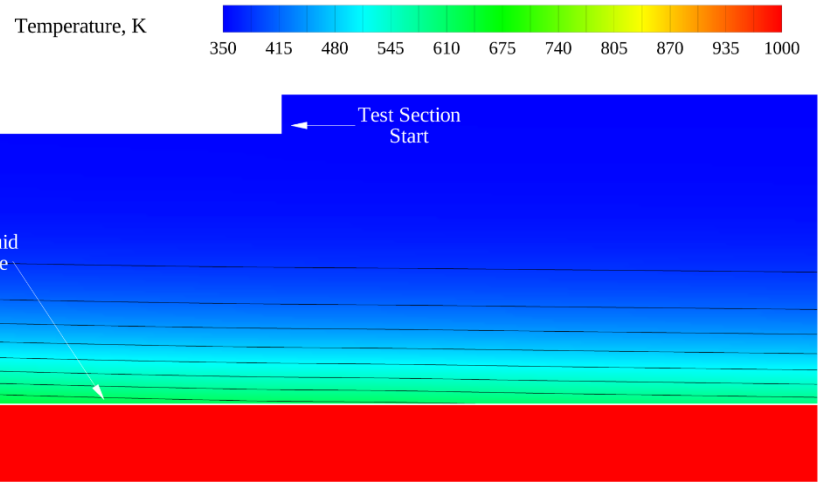

- Flowfield is only impacted close to the wall
- Solid largely remains at the initial temperature

Temperature Profile

Start of Test Section 2

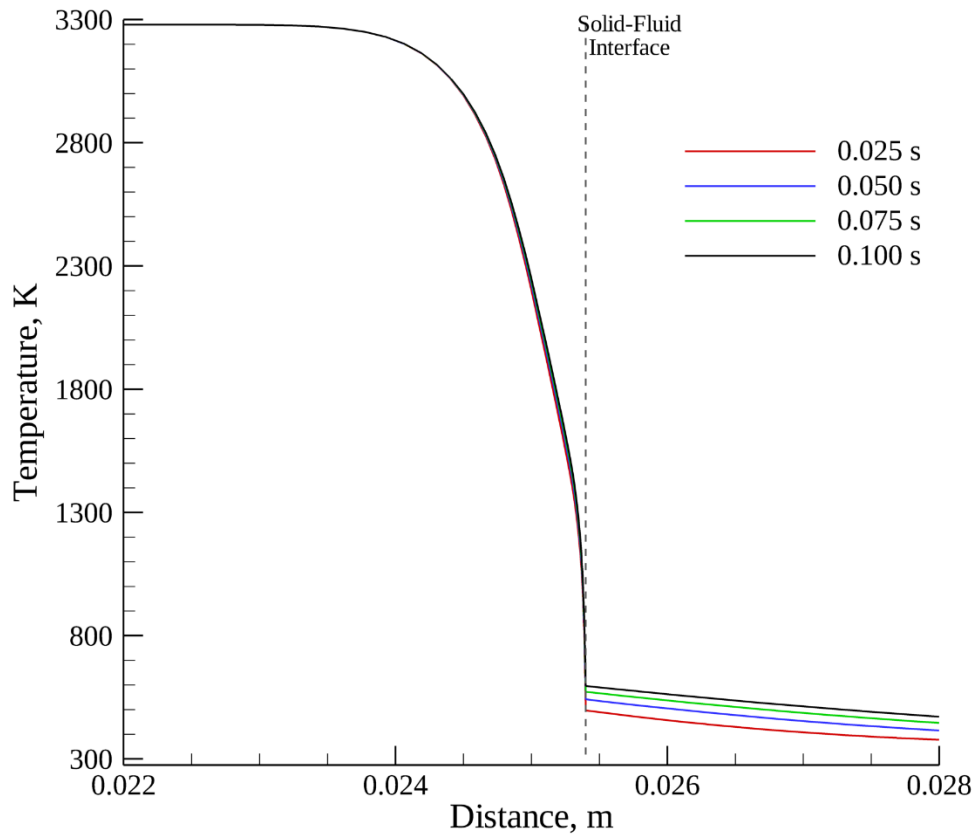

Start of Test Section 5

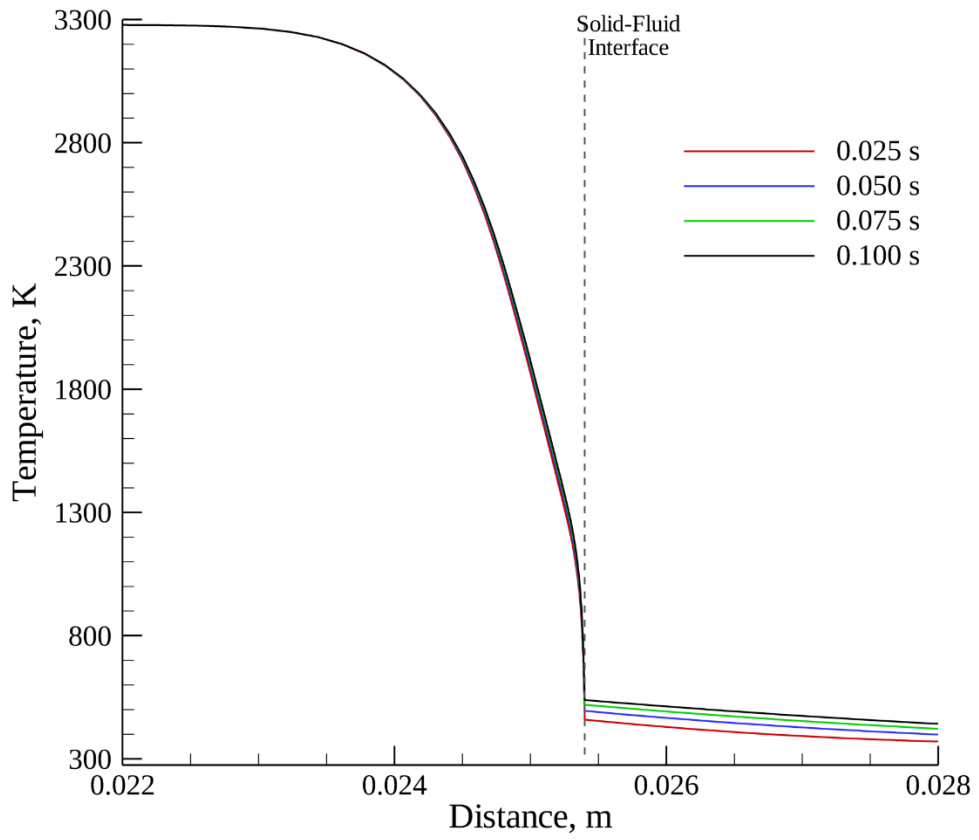

Species Profiles

Start of Test Section 2

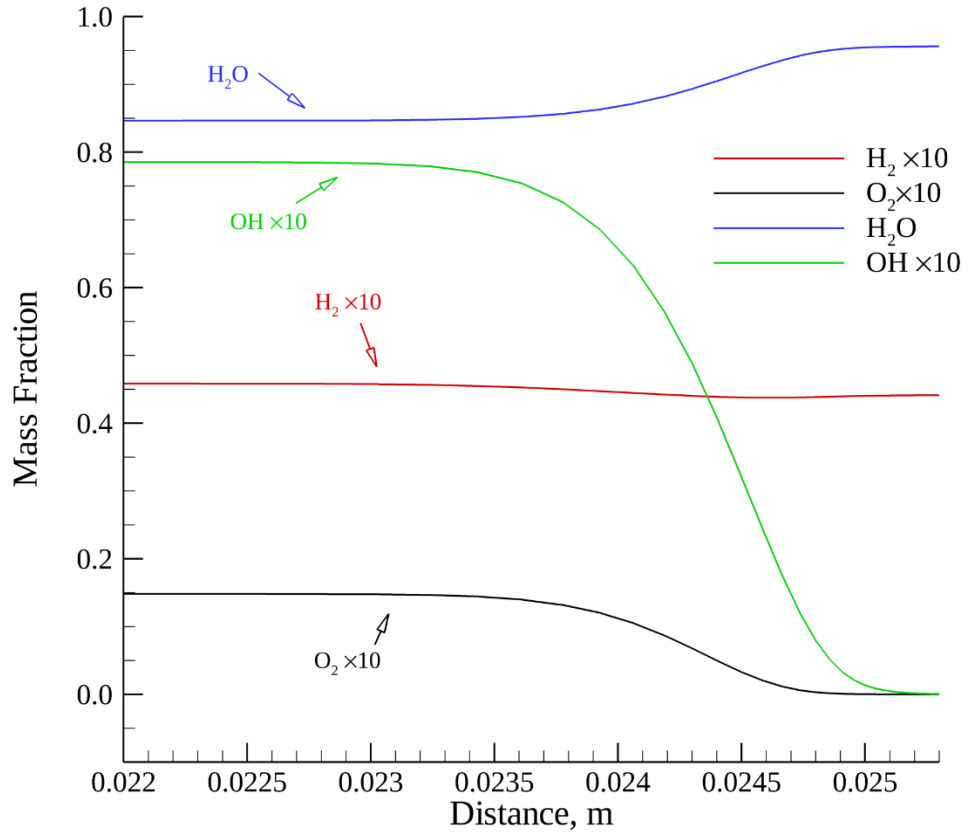

Start of Test Section 5

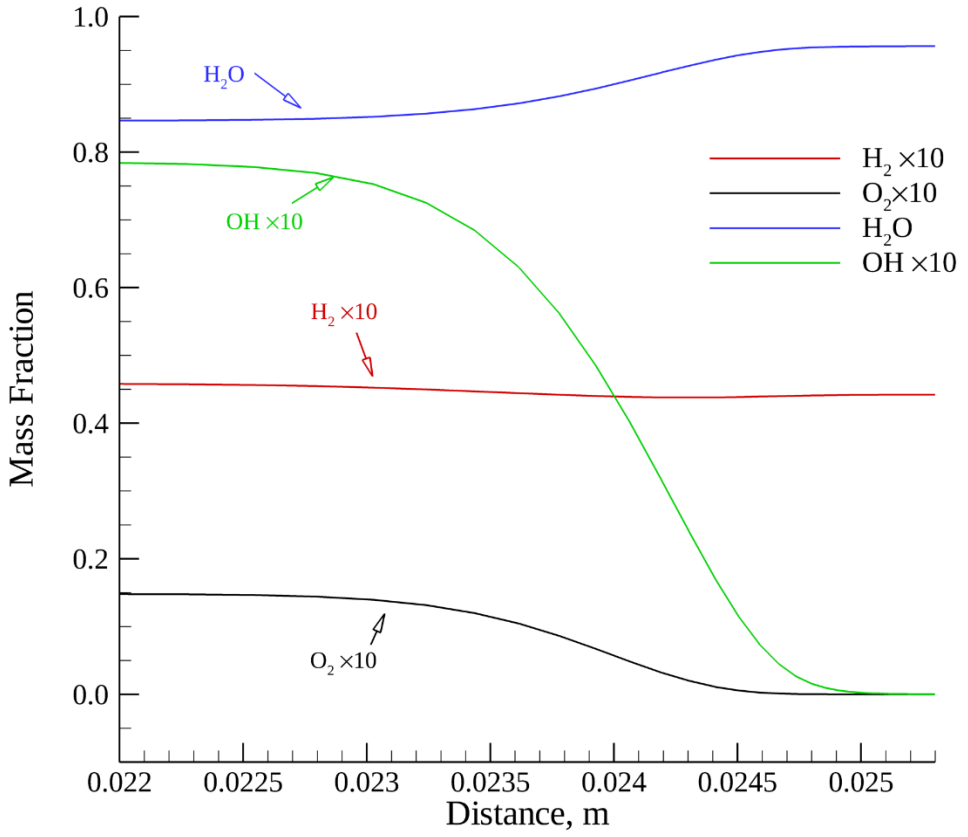

Thermal Conductivity

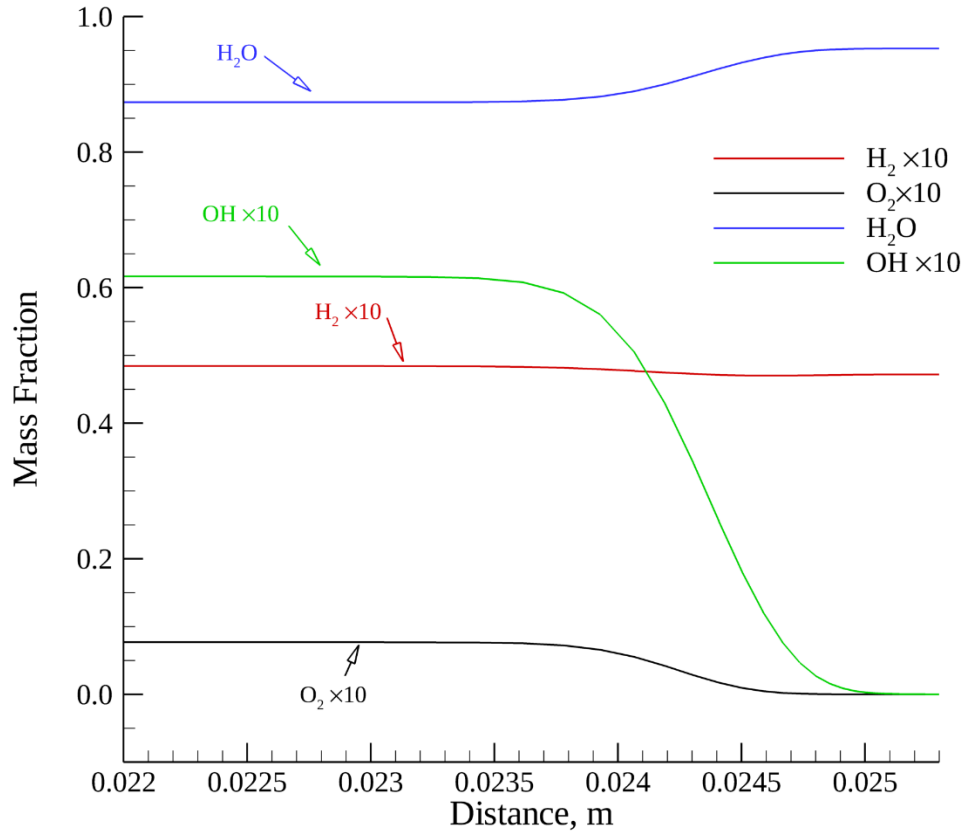

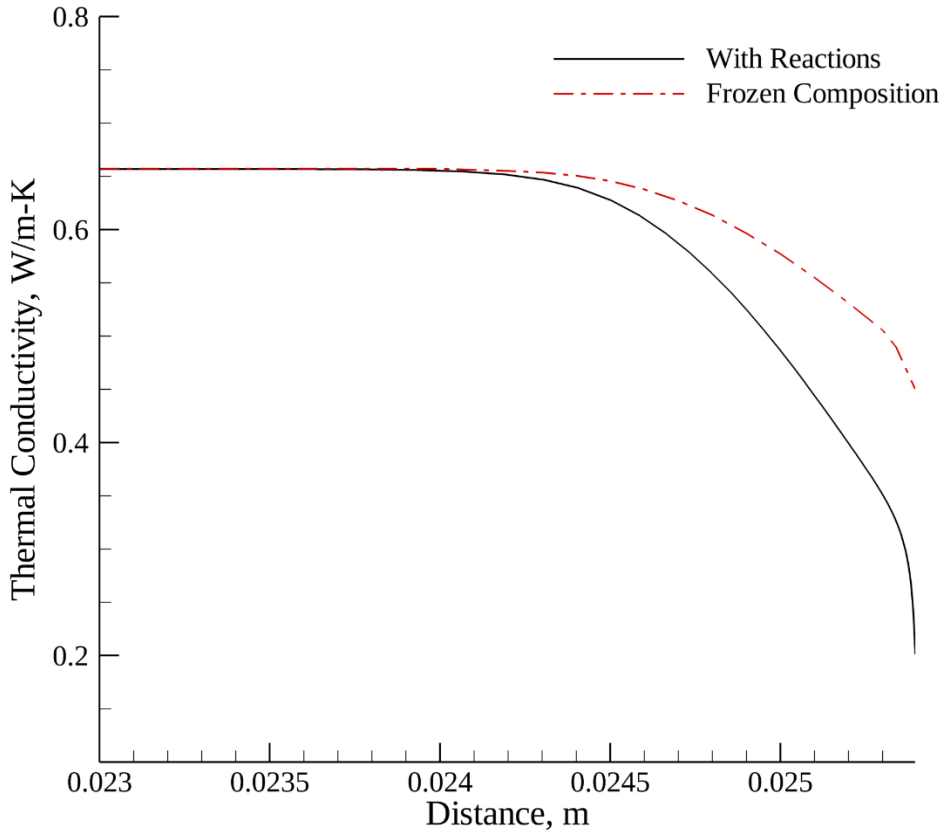

Condition 2

- Why is condition 2 an outlier?
  - Higher O/F ratio
    - Combusted gas temperature and products is largely similar
  - Low surface temperature
    - Is this too close to the starting point that the simulation is inaccurate?
    - Dependence on initial conditions
    - Increased experimental uncertainty
- Table to the left shows the heat flux computed from the computation at higher surface temperatures
  - Value approaches the experimental value when the surface temperature is increased

Surface Temp, K	Heat Flux, btu/in²-s	Error
459.26	6.6	Exp.
459.26	7.238	9.67%
480.00	6.956	5.39%
500.00	6.774	2.64%
520.00	6.650	0.76%

Summary

- Summary:
  - A conjugate heat transfer tool was developed using the GEMS CFD code
  - The tool's ability to capture unsteady conduction was verified
  - The conjugate heat transfer capability was tested against a liquid rocket engine test case
  - The predicted heat flux agreed within 4% for 3 of the 4 operating conditions

- Future Work:
  - Incorporate a wall model to reduced the simulation cost